Received: 8 June 2021 | Revised: 20 July 2021 | Accepted: 15 August 2021

DOI: 10.1002/jbio.202100173

RESEARCH ARTICLE

JOURNAL OF BIOPHOTONICS

Monitoring aging-associated structural alterations in *Caenorhabditis elegans* striated muscles via polarization-dependent second-harmonic generation measurements

Vassilis Tsafas[1,2] | **Konstantina Giouroukou**[1,2] | **Konstantinos Kounakis**[3,4] | **Meropi Mari**[1] | **Costas Fotakis**[1,2] | **Nektarios Tavernarakis**[3,4] | **George Filippidis**[1*]

[1]Institute of Electronic Structure and Laser, Foundation for Research and Technology, Heraklion, Greece

[2]Department of Physics, University of Crete, Heraklion, Greece

[3]Institute of Molecular Biology and Biotechnology, Foundation for Research and Technology, Heraklion, Greece

[4]Medical School, University of Crete, Heraklion, Greece

***Correspondence**
Dr. George Filippidis, Institute of Electronic Structure and Laser, Foundation for Research and Technology, Heraklion 71110, Crete, Greece.
Email: filip@iesl.forth.gr

Funding information
Laserlab-Europe, Grant/Award Number: 871124; HFRI; General Secretariat for Research and Technology; Hellenic Foundation for Research and Innovation

Abstract

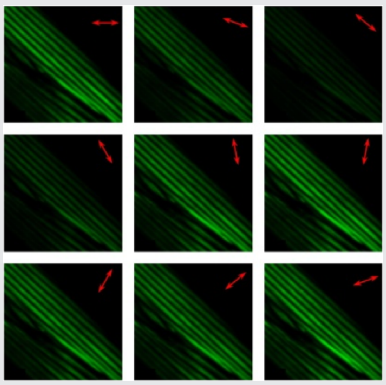

The in-vivo elucidation of the molecular mechanisms underlying muscles dysfunction due to aging via non-invasive label free imaging techniques is an important issue with high biological significance. In this study, polarization-dependent second-harmonic generation (PSHG) was used to evaluate structural alterations in the striated muscles during *Caenorhabditis elegans* lifespan. Young and old wild-type animals were irradiated. The obtained results showed that it was not feasible to detect differences in the structure of myosin that could be correlated with the aging of the worms, via the implementation of the classical, widely used, cylindrical symmetry model and the calculation of the SHG anisotropy values. A trigonal symmetry model improved the extracted results; however, the best outcome was originated from the application of a general model. Myosin structural modifications were monitored via the estimation of the difference in spectral phases derived from discrete Fourier transform analysis. Age classification of the nematodes was achieved by employing both models, proving the usefulness of the usage of PSHG microscopy as a potential diagnostic tool for the investigation of muscle diseases.

KEYWORDS

aging, *Caenorhabditis elegans*, myosin, polarization-dependent measurements, second harmonic generation imaging, striated muscles

1 | INTRODUCTION

Aging is directly related to the gradual loss of muscle mass and strength of the human musculoskeletal system. The effect of aging on muscles is called sarcopenia. Sarcopenia syndrome is age-related [1] and occurs in healthy adults over the age of 50. It represents a high risk for physical disability due to gradual muscle loss [2]. On a microscopic scale, the pathological causes of sarcopenia are due to changes in both the composition and function

of the molecules and proteins that are structural elements of the sarcomere. Biochemical studies have revealed that the myosin molecule undergoes molecular changes over time, thus contributing to the development of the syndrome [2]. Moreover, sarcopenia also occurs at the nematode *Caenorhabditis elegans*, because its body wall muscles are known to deteriorate with aging [3, 4].

In our study, polarization-dependent second-harmonic generation (PSHG) microscopy was employed to extract quantitative information for the changes that occur in the structure of the myosin molecules of *C. elegans* samples during aging. In particular, the body wall muscles of *C. elegans*, which consist of striated muscles, were investigated. Striated muscles are formed from multiple sarcomeres and are similar to human skeletal muscles [5]. Myosin molecules are some of the main building blocks of the sarcomeres. Each molecule consists of two heavy chains, which fold and form a double helix [6]. Myosin is an ideal emitter of high SHG signals due to its non-centrosymmetric structure [7, 8].

SHG is a non-linear coherent scattering phenomenon, which means that no energy is absorbed from the sample, making this imaging technique suitable for non-destructive in-vivo biological studies. Advantages of SHG include the high lateral and axial resolution, which gives the ability for observation at a cellular level, increased penetration depth and the capability for intrinsic three-dimensional sectioning of the irradiated specimens. In addition, SHG records label-free images from unstained samples while minimizing photobleaching and phototoxicity effects. PSHG imaging is an optical microscopy technique capable of quantifying molecular structural changes occurring even below the diffraction limit [9, 10]. Relevant information about the orientation of the sample's SHG emitters at molecular and supramolecular scale can be extracted [11, 12]. PSHG imaging has been used to characterize the molecular architecture of main endogenous sources of contrast, such as collagen and myosin, in tissues [13, 14].

Studies have used PSHG measurements for the functional imaging of muscle cells and the in-vivo monitoring of conformational changes in myosin [15, 16]. Moreover, structural modifications of cardiac myosin filaments have been detected, and the discrimination of a- and b-myosin in cardiac samples via PSHG was possible [17, 18]. In the current work, we used PSHG imaging microscopy to measure aging-related myosin structural modifications in the striated muscles of *C. elegans* samples. A discrete Fourier transform (DFT) algorithm for the fast SHG signal analysis has been employed for probing myosin structural alterations. Based on the classical cylindrical mathematical symmetry model, it was not feasible to extract significant changes in the calculated anisotropy parameter values, due to aging of the nematodes. Subsequently, a trigonal symmetry and a general mathematical model, which characterizes specimens with unknown structure and is not based on symmetries, were employed for the PSHG data analysis. It was demonstrated that the worms were better described via the implementation of these two models while the discrimination of the younger from the older animals was also achieved.

2 | MATERIALS AND METHODS

2.1 | Biological samples

The broad ranges of genetic and molecular techniques applicable in the *C. elegans* model organism allow a unique line of investigation into fundamental problems in biology. The transparency of the organism makes it an ideal model system for in-vivo visualization experiments. Thus, we opted to implement the non-destructive method of PSHG on living, anesthetized animals to ensure our results match reality as close as possible. Specifically, we followed standard procedures for *C. elegans* strain maintenance, crosses and other genetic manipulations [19]. Nematode rearing temperature was kept at 20°C. Before each experiment, adult animals were anesthetized by immersing to an anesthetic mixture with a final volume of 20 μL (15 μL tetramisole sulphate 100 mM, 5 μL sodium azide [NaN_3] 20 mM), and subsequently, they were mounted on thin glass slides. In this study, wild-type worms at the first, sixth and ninth day of adulthood were imaged.

2.2 | PSHG setup

In this work, SHG signals were collected from a custom-made experimental setup, which has been previously described in detail [10, 20]. A femtosecond Yb-based laser oscillator (1028 nm, 200 fs, 50 MHz, 1 W, Amplitude Systemes) was used for the irradiation of the nematodes. The laser was guided into a modified Nikon upright microscope. The power at the focal plane was adjusted with use of neutral density filters placed in front of the laser output. The energy per pulse at the sample plane was 0.5 nJ. A phase retardation wave plate (WPH05ME; Thorlabs) was employed for the rotation of the laser polarization by a specific angle in order to create PSHG data sets. The extinction ratio, using cross polarization measurements at the sample plane, was measured to be higher than 25:1 for all linear polarization orientations.

An objective lens (Carl Zeiss) with a moderate numerical aperture (NA) of 0.85 was used to focus the laser beam onto the sample. The raster (xy) scanning procedure was performed with a pair of silver-coated galvanometric mirrors (Cambridge Tech). The samples were fitted into a motorized xyz translation stage (Standa). The proper focal plane and the desired specimen area for the performance of the raster scanning were selected with this stage. LabVIEW interface controlled both scanning and data acquisition procedures. SHG signals were collected in forward direction using a photomultiplier tube (PMT Hamamatsu H9305-04) and a second objective lens. A bandpass interference filter (Semrock 514) and a short pass filter (Semrock 720) were placed at the PMT input to cut off the transmitted laser light and solely detected SHG signals from the samples. Typical time duration for obtaining a single 2D 500×500 pixels ($90 \times 90\ \mu m^2$) SHG image was 1 second. Each pixel is a square with 0.18 μm side. To improve the signal-to-noise ratio (SNR), 10 scans were realized for each image. For each sample, as will be discussed in detail in Section 2.4, 18 averaged images constitute a complete PSHG dataset. In addition, this custom-built imaging apparatus provided the ability to lighting the biological sample with an illumination source (white lamp) while the observation occurred through a charged-coupled device sensor (PLA662; PixeLINK) attached to the camera port of the microscope.

In our work, the striated muscles of both young and old animals provide high SHG signals indicating structures without inversion symmetry centre. Specimens, where movement was observed during their irradiation or muscle contractions, were not included in the study.

2.3 | PSHG theory

Myosin thick filaments, which are the main sources of high SHG from *C. elegans* body striated muscles [8], are assumed to be arranged in a cylindrically symmetric distribution along with muscle fibre and parallel to it [8]. For this reason, the modulation of the SHG signal produced by the *C. elegans* body muscles, with respect to the rotation of the incident linear polarization of the excitation laser, is described by the following equation [14, 21, 22]:

$$I_{SHG} = E \cdot \left\{ (\sin[2(a-f)])^2 + \left[(\sin(a-f))^2 + B \cdot (\cos(a-f))^2 \right]^2 \right\}, \quad (1)$$

where E is an overall multiplication factor, f denotes the angle between the initial polarization of the laser and the projection of the sample's symmetry axis onto the polarization plane and a is the rotation angle of the laser linear polarization due to the half-wave plate. Furthermore, the factor B of Equation (1) is called anisotropy parameter and is a function of the only nonvanishing and independent second-order tensor elements. In our case where the sample's symmetry axis lies onto the polarization plane (we assume that the laser propagation axis is almost perpendicular to the muscle fibre axis), anisotropy parameter B is defined as [10]:

$$B = \frac{\chi_{33}}{\chi_{31}}, \quad (2)$$

while in the macroscopic point of view, B can be expressed as the ratio of the SHG electric fields when the linear polarization is parallel ($a\text{-}f = 0°$) and perpendicular ($a\text{-}f = 90°$) to the sample's symmetry axis.

$$B = \sqrt{\frac{I_{SHG}^{\parallel}}{I_{SHG}^{\perp}}} = \frac{E_{SHG}^{\parallel}}{E_{SHG}^{\perp}}. \quad (3)$$

For this geometry, as Equation (4) shows, B is also related with the effective angle θ_e, which is the most probable angle between the thick filament's SHG emitters and sample's symmetry axis. In cases like myosin and collagen, the effective angle θ_e is in agreement with the pitch angle of their helices [14].

$$\cos^2(\theta_e) = \frac{B}{2+B}. \quad (4)$$

The Fourier decomposition of Equation (1) is [16]:

$$I_{SHG} = c_0 + c_2 \cdot \cos(2 \cdot (a-f)) + c_4 \cdot \cos(4 \cdot (a-f)), \quad (5)$$

where,

$$B = \sqrt{\frac{c_0 + c_2 + c_4}{c_0 - c_2 + c_4}}. \quad (6)$$

The form of Equation (5) enables the calculation of c_0, c_2 and c_4 coefficients (therefore, B) and angle f through DFT of I_{SHG} values for several different polarization angles a [16, 23]. The advantage of DFT is that the computational time required, in order to calculate the anisotropy parameter B and angle f for all of the 500×500 pixels of one image, is 10^4 orders of magnitude less compared with the utilization of a nonlinear fitting algorithm needed by Equation (1). Specifically, the time needed for data processing with the DFT algorithm is 1 second.

Equation (5) requires both of the cosine terms to have the same value for angle f. The most general form of I_{SHG} dependence with respect to the angle a is [24, 25]:

$$I_{SHG} = b_0 + b_2 \cdot \cos(2 \cdot a) + b_4 \cdot \cos(4 \cdot a) + d_2 \cdot \sin(2 \cdot a) + d_4 \cdot \sin(4 \cdot a), \quad (7)$$

which can be written as:

$$I_{SHG} = b_0 + b_2' \cdot \cos(2 \cdot (a - f_2)) + b_4' \cdot \cos(4 \cdot (a - f_4)), \quad (8)$$

and in this form, it is clear that the difference is compared with Equation (5). In Equation (8), no symmetry axis has been assumed; thus, angles f_2 and f_4 (spectral phases) may differ. This will be pointed out analytically in the next session.

If SHG emitters are arranged with the polar trigonal symmetry 3m (referred from now on for simplicity just as trigonal), then the generated SHG signal as a function of the previously defined angles a and f takes the following form [26]:

$$I_{SHG} = E \cdot \left\{ \left(\chi_{22} \cdot (\sin(a - f))^2 + \chi_{15} \cdot \sin[2(a - f)] \right)^2 + \left[\chi_{31} \cdot (\sin(a - f))^2 + \chi_{33} \cdot (\cos(a - f))^2 \right]^2 \right\}. \quad (9)$$

In the case where χ_{22} equals to zero and the sample does not absorb the incident radiation, (thus, Kleinman symmetry is valid, and χ_{15} is equal to χ_{31}), Equation (9) takes the form of Equation (1). This means that cylindrical symmetry is a specific case of trigonal symmetry, and the ratio of the absolute value of χ_{22} divided by χ_{31} comprises a measure of the balance between these two symmetries. This ratio, denoted as S (symmetry parameter), and its increase correspond to the dominance of trigonal symmetry against the cylindrical one [27, 28].

Via simple trigonometric identities, Equation (9) can also be written in the general form of Equation (7) as:

$$I_{SHG} = b_0 + b_2 \cdot \cos(2 \cdot (a - f)) + b_4 \cdot \cos(4 \cdot (a - f)) + d_2 \cdot \sin(2 \cdot (a - f)) + d_4 \cdot \sin(4 \cdot (a - f)), \quad (10)$$

where:

$$b_0 = E\left[\frac{3 \cdot (x_{22}^2 + x_{31}^2 + x_{33}^2)}{8} + \frac{x_{15}^2}{2} + \frac{x_{31} \cdot x_{33}}{4} \right], \quad (11)$$

$$b_2 = E\left[\frac{x_{33}^2 - x_{31}^2 - x_{22}^2}{2} \right], \quad (12)$$

$$d_2 = E[x_{22} \cdot x_{15}], \quad (13)$$

$$b_4 = E\left[\frac{x_{22}^2 + x_{31}^2 + x_{33}^2 - 4 \cdot x_{15}^2 - 2 \cdot x_{31} \cdot x_{33}}{8} \right], \quad (14)$$

$$d_4 = E\left[\frac{-x_{22} \cdot x_{15}}{2} \right]. \quad (15)$$

Finally, Equation (10) can be re-expressed based on the form of Equation (8) as:

$$I_{SHG} = b_0 + b_2' \cdot \cos(2 \cdot (a - [f - \Delta f_2])) + b_4' \cdot \cos(4 \cdot (a - [f - \Delta f_4])), \quad (16)$$

where:

$$\Delta f_2 = \frac{\operatorname{atan}\left[\frac{2 \cdot S \cdot \frac{x_{15}}{x_{31}}}{S^2 - \left(\frac{x_{33}}{x_{31}} \right)^2 + 1} \right]}{2}, \quad (17)$$

and

$$\Delta f_4 = \frac{\operatorname{atan}\left[\frac{4 \cdot S \cdot \frac{x_{15}}{x_{31}}}{4\left(\frac{x_{15}}{x_{31}} \right)^2 + 2 \cdot \frac{x_{33}}{x_{31}} - S^2 - \left(\frac{x_{33}}{x_{31}} \right)^2 - 1} \right]}{4}. \quad (18)$$

For the trigonal symmetry case, the physical meaning behind the difference in spectral phases (angles f_2 and f_4) from Equation (8) is clear now. These angles, which can be computed through the DFT of SHG signal, are equal with the angle f minus Δf_2 and Δf_4, respectively. Equations (17) and (18) show that these Δf values depend on S. Figure 1 presents that the increase of S also expands the difference between f_2 and f_4. Thus, a potential increase in the difference of these two angles is an indicator of the presence of trigonal rather than cylindrical symmetry in a system.

2.4 | PSHG data analysis

For each sample, 18 2D SHG images of the same area were recorded, rotating the laser's linear polarization by

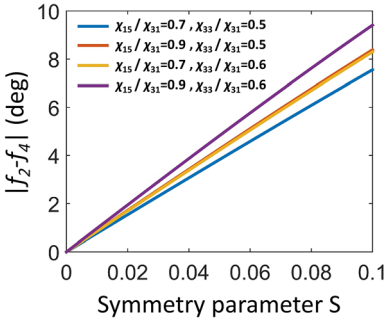

FIGURE 1 Plot diagram of the absolute difference between f_2 and f_4 based on Equations (17) and (18) for different typical values of χ_{15}/χ_{31} and χ_{33}/χ_{31} as symmetry parameter S increases

10° each time (a = 0°-170°) and thus creating a 3D matrix (PSHG matrix) with dimensions 500 × 500 × 18. For the cylindrical symmetry model for each pixel area (500 × 500), the values of angle f, coefficients c from Equation (5) and, subsequently, the value of B through Equation (6), were calculated via the application of DFT analysis along the third dimension of the PSHG matrix. However, due to the in-vivo nature of our experiments, small movements of the samples were possible during PSHG measurements. To verify the validity of our analysis, the 18 recorded SHG images were first aligned through Fiji software to ensure that the modulation of the non-linear signal from a pixel area comes from the rotation of the incident polarization. Images from samples that were not sufficiently aligned with the software were discarded.

First, a specially constructed algorithm, that was designed and programmed in MATLAB environment, computed the coefficients c_0 and c_2 and the angle f (indicated from now on as f_c, due to the cylindrical symmetry approach) of the left cosine term of Equation (5) by applying DFT along the third dimension of the PSHG matrix. In particular, the algorithm computes the coefficients b_2 and d_2 of Equation (7) via DFT analysis. The coefficient c_2 can be equal with the positive or the negative square root $\sqrt{{b_2}^2+{d_2}^2}$. The way in which this uncertainty is avoided is based on the appropriate c_2 sign selection as described by Wasik et al. [29]. In our case due to the fact that the expected anisotropy parameter is significantly smaller than the unit [8, 14], the negative sign of c_2 has been chosen [9], whereas angle f_c calculated via the built-in Matlab function atan2 (f_c = atan2(d_2/c_2, b_2/c_2)/2). The range of f_c based on this analysis is from −90° to 90°, because the output of atan2 function is from −180° to 180°, and there is a division by 2. Afterwards, the algorithm computed the last coefficient c_4 by assuming as a constant the already known value for angle f_c of the right cosine term and taking into account that the period of Equation (5) is 180° ($c_4 = \frac{2}{18}\cdot\sum_{i=1}^{i=18} I_{SHG}(i)\cdot\cos\left(4\cdot\left(\frac{\pi}{18}\cdot(i-1)-f_c^{rads}\right)\right)$).

In the interest of calculating average values for the anisotropy parameter B (<B>) and angle f_c (<f_c>), erroneous pixels, like noise pixels, which were not in line with Equation (5), had to be excluded. In this study, a threshold value was used as a filtering criterion as referred in the literature [10, 12] for the determination of coefficient R^2. Pixels below the threshold value were excluded from further processing. Specifically, the threshold value of 0.90 was set, in order to ensure that the results fit into the model while at the same time maintaining a high enough number of pixels for the statistical analysis.

The next step was the introduction of the general model for the data analysis. This was accomplished via the implementation of an algorithm computing the coefficients b_4 and d_4 of Equation (7) and through them the coefficient b_4' and angle f_4 of Equation (8) by applying DFT again along the third dimension of the PSHG matrix.

There is no need to estimate the values of the coefficients b_0, b_2' or angle f_2 of Equation (8) since the way they are calculated by DFT is identical to that of c_0, c_2 and angle f_c of Equation (5). This is valid under the logical assumption that the sign of b_2, which determines the sign of b_2', remains negative for small deviations from the cylindrical symmetry. For example, as Equation (12) depicts, this assumption is always valid for trigonal symmetry. However, the recalculation of R^2 values is necessary.

For the calculation of b_4', the negative square root of ${b_4}^2+{d_4}^2$ is selected since the expected sign of b_4 is also negative, similarly to the aforementioned b_2 case. Subsequently, the built-in Matlab function atan2 is used for the calculation of f_4 (f_4 = atan2(d_4/b_4', b_4/b_4')/4). As previously mentioned for the f_2 case, the range of f_4 based on this analysis is limited from −45° to 45°. Moreover, the difference between f_2 and f_4, as will be discussed later, is one of the main key points of this study. For the calculation of this difference, the range of these two angles must be equal. This can be achieved by properly adding or subtracting an extra 90° angle (which is the period of the corresponding cosine) to f_4 if the difference f_2-f_4 is greater or lower than 45° and −45°, respectively, since for small deviations from the cylindrical symmetry, the absolute value of this difference is not expected to exceed the 45°.

As discussed previously, Equation (9) describes samples where trigonal symmetry is dominant. Equation (9) can be written in the form of Equation (16) where the

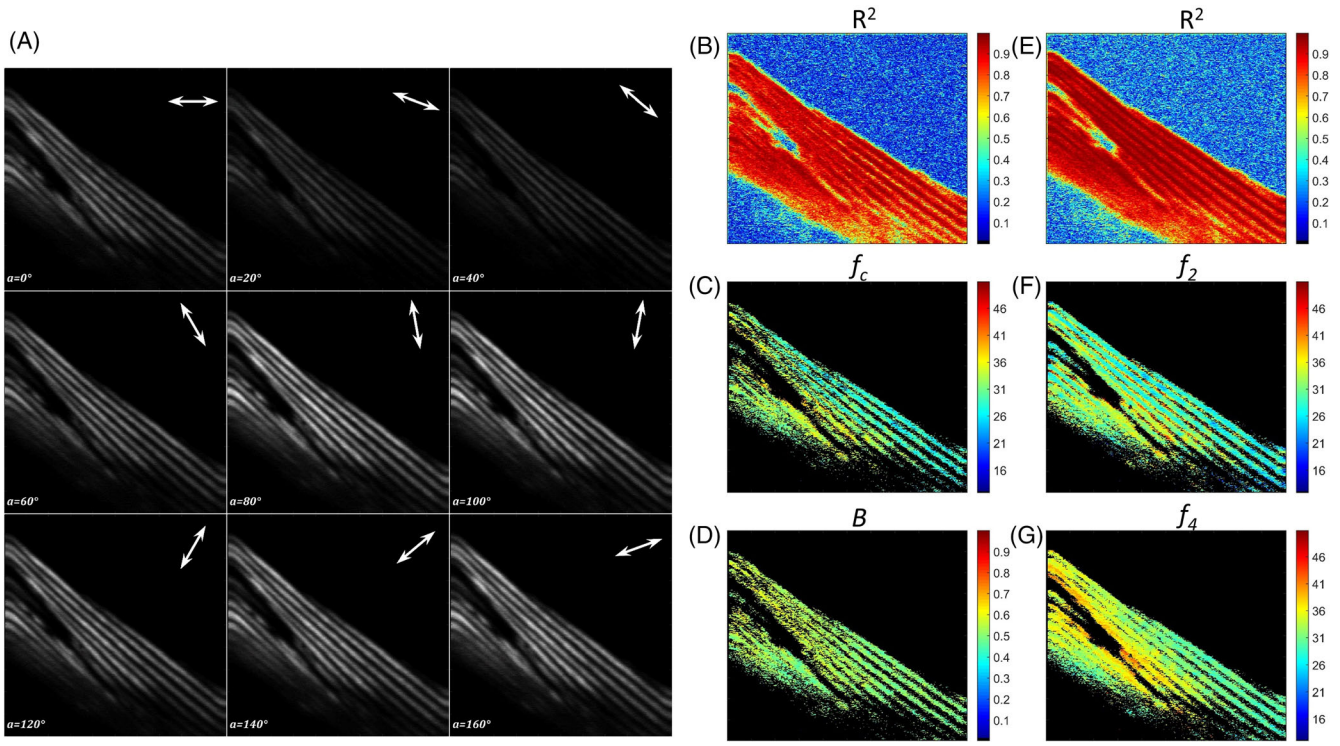

FIGURE 2 Results of DFT analysis, B-D, based on Equation (5) and, E-G, based on Equation (8) for the PSHG dataset recorded from the middle body part of a 1-day old sample. A, Nine of the 18 PSHG dataset images. Each sub-image depicts the same area, and the brightness is analogue to the SHG recorded signals. The white arrow corresponds to the laser's linear polarization into the sample plane. The value of angle a is displayed at the bottom left of each sub-image. B,E, The colour of each pixel corresponds to the value of R^2 calculated for this pixel through the DFT analysis. C,D,F,G, Pixels with $R^2 < 0.9$ have been excluded from further analysis and were displayed in black colour. C, Angle f_c computed values. D, Anisotropy parameter B computed values. F,G, Calculated values for angles f_2 and f_4, respectively

coefficients b_0, b_2', b_4', f_2 and f_4 can be calculated via DFT analysis. However, for specimens with unknown structure, the DFT analysis cannot confidently provide information about Equation (9) parameters (E, f, χ_{22}, χ_{15}, χ_{31} and χ_{33}). As mentioned in the previous section, the Fourier form of Equation (7) can describe the SHG signal modulation with respect to the angle of the laser polarization, even in the case that all the second-order tensor elements are independent and non-zero. This means that the b_0, b_2, b_4, d_2 and d_4 coefficients, which are the only results that DFT provides, in general, may be affected by tensor elements that the Equations (11)–(15) of the trigonal symmetry do not take into account. For that reason and in order to have an estimation of Equation (9) parameters (trigonal symmetry model), it was chosen to complete the analysis by fitting the SHG modulation on Equation (9) for all the pixels areas of each sample. An extra factor called 'ratio parameter' was also calculated for providing quantitative information. The value of this parameter was defined as the number of pixels with $R^2 > 0.9$ divided by the total number of pixels in the myosin sample area [10]. Introducing this factor to the aforementioned fitting analysis and the two DFT methods provides a quantitative measure for the ability of the extracted results to sufficiently describe the PSHG data of each sample.

Figure 2 depicts some representative results of our DFT analysis algorithm based on the cylindrical and the general model, in a wild-type day-1 adult animal. Measurements were recorded from the striated muscles in the mid body region of the worm.

For the cylindrical symmetry case, the mean values of B ($\langle B \rangle$) and angle f_c ($\langle f_c \rangle$) as well as the SDs of them, deriving from pixels with $R^2 > 0.9$, were calculated to be 0.53 ± 0.04 and $31.5^\circ \pm 3.4^\circ$, respectively. In our case, due to the fact that a sample-based analysis has been followed, the precision of $\langle B \rangle$ and $\langle f_c \rangle$ is determined as the SD of the corresponding values resulting from all the image pixels. It is worth to be mentioned that, recent studies present an alternative, new method where the precision of the calculated B and f_c values can be estimated for each pixel [29, 30].

The extracted value of $\langle B \rangle$ considering Equation (3) matches with the lower brightness of Figure 2A for $a = 40^\circ$ (incoming polarization parallel to the sample symmetry axis) divided to $a = 140^\circ$ where the polarization is perpendicular. In addition, through Equation (4),

the value of <*B*> corresponds to an effective angle of θ_e around $63^\circ \pm 1^\circ$. We have to note that the X-ray measured myosin helix angle is 68° [14]. Moreover, the calculated value of angle $<f_c>$ is close to the minimum expected value of 33° considering that the angle between the direction of the initial laser's polarization (Figure 2A, $a = 0^\circ$) and fibre's axis is around 40° and that myosin thick filaments are at an angle of 5°-7° to the muscle fibre [31].

By comparing Figure 2C and Figure 2F, it can be noticed that the calculated values of angles f_c and f_2 are similar. However, in the second case, there is an increase in the number of pixels that present values with $R^2 > 0.9$, and the same holds true when comparing Figure 2E with Figure 2B. This increase is mainly due to the fact that the values of angle f_4, calculated from the general model of Equation (8), differ from those of f_2 as shown in Figure 2G,F, respectively. Furthermore, the increase of R^2 can be expressed quantitatively through the estimation of the ratio parameter values. The ratio parameter was calculated to be 0.51 and 0.79 for the cylindrical symmetry and the general model, respectively.

2.5 | Statistical analysis

For multi-group comparisons, two-tailed unpaired Student *t* test was applied. *P* values <.05 were considered significant (*). Twelve animals were irradiated for each age group.

3 | RESULTS

PSHG measurements were performed in an attempt to monitor potential structural changes in striated muscles of *C. elegans* samples during aging. Worms were irradiated at different time points in order to cover a wide range of the animal life span. The target of the present study was the use of a high resolution, label free, non-destructive imaging technique as a novel diagnostic tool and the identification of the best approach for data analysis for revealing sub cellular muscular changes during animals aging. Initially, the classical cylindrical model that is widely used for the in-vivo monitoring of alterations in myosin [15, 16] was employed for the analysis of the extracted PSHG data and the age classification of the samples. Figure 3 presents the results of the implementation of the algorithm to a middle-aged *C. elegans* sample (6 days) while Figure 4 shows an old (9 days) worm. Measurements were recorded from the mid body part of the worms where the striated muscles are located.

In order to examine potential *B* value variations during the aging of the *C. elegans*, the average values of <*B*> for the three age groups (1 day, 6 days and 9 days of adulthood) were calculated via our PSHG analysis based on Equations (5) and (6). Twelve samples for each age category were tested. The obtained results, presented in Figure 5, depict that no significant difference was detected in the extracted *B* parameter values due to aging of the samples. Thus, it is not feasible to obtain information related to structural alterations in the striated muscles of the worms due to aging via this measure. Thus, after the inability of the cylindrical model to detect changes during *C. elegans* aging, the trigonal symmetry was investigated, and a general model was also applied for acquiring improved results.

Through our DFT analysis based on Equation (8) that represents the general model, and the fitting procedure in Equation (9) that indicates the trigonal symmetry model it was observed that the difference between the angles f_2 and f_4 was increased in the older age group.

Figure 6A presents the average absolute difference in the values between the angles f_2 and f_4 (DIF) calculated with two different ways. In both cases, by implementing DFT analysis based on Equation (8) and by using fitting procedure based on Equation (9), older *C. elegans* samples present higher values compared to the younger ones. However, the mean DIF values showed a statistically significant increase for the 9d compared to the 1d samples only for the analysis derived from the general model. Figure 6B depicts the calculated *S* mean values. Higher *S* values are an indicator that the trigonal symmetry is promoted against the cylindrical one. The DIF rise of the older specimens is accompanied by an increase in *S* values (Figure 6). Thus, the recorded results show that the dominance of trigonal versus the cylindrical symmetry is enhanced in the striated muscles during the aging of *C. elegans*.

In an attempt to investigate the symmetry that better describes the myosin alterations that occur during the aging of the worms, the ratio parameter values for the three approaches (cylindrical, trigonal and general models) were estimated. Figure 7 presents the mean ratio values for the 1d, 6d and 9d samples. This figure demonstrates that the trigonal model is preferable for the description of the three age groups in comparison to the classical cylindrical symmetry model. Moreover, Figure 7 shows that the aging procedure is better delineated by employing DFT analysis based on Equation (8) (general model) rather than the fitting procedure based on Equation (9) that represents the trigonal symmetry model.

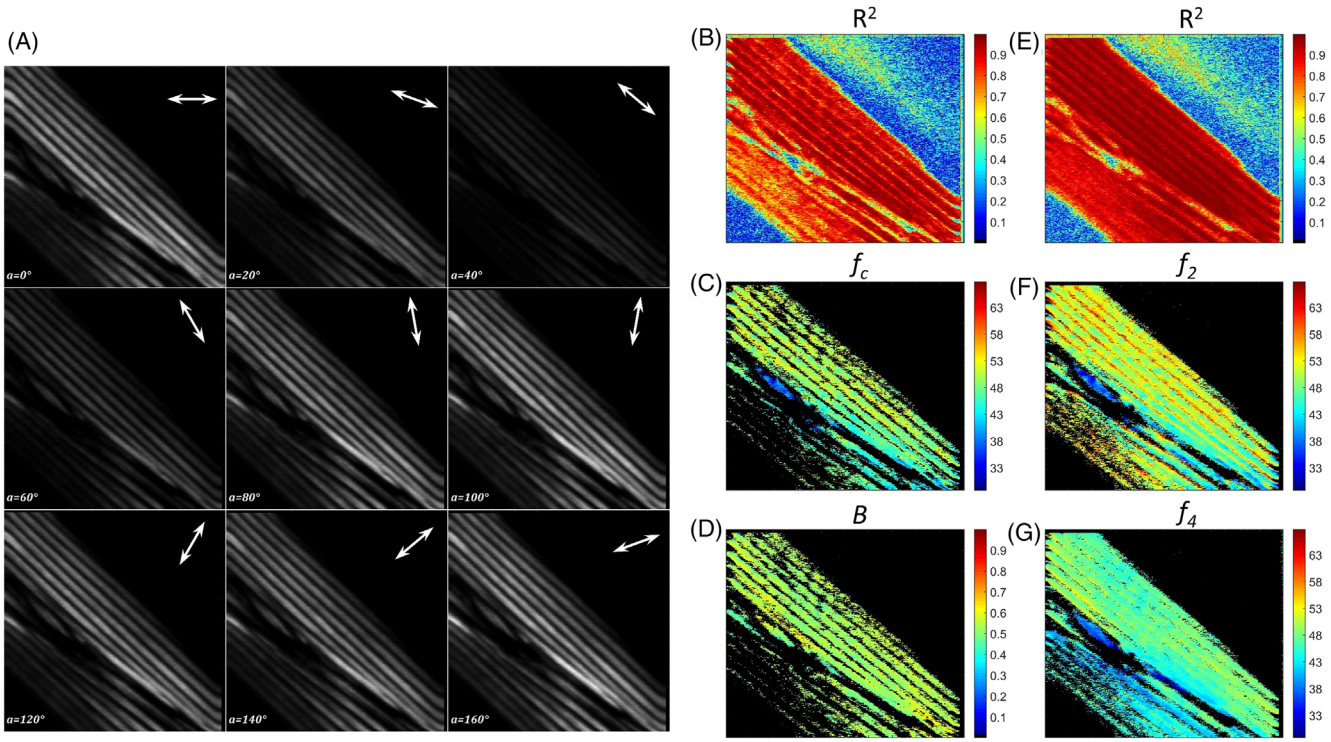

FIGURE 3 Results of DFT analysis, B-D, based on Equation (5) and, E-G, based on Equation (8) for the PSHG dataset from a 6-days old sample. A, Nine of 18 PSHG dataset images. The white arrow corresponds again to the laser's linear polarization into the sample plane, and the value of angle a is displayed at the bottom left of each sub-image. B,E, The colour of each pixel corresponds to the value of R^2 calculated for this pixel through the DFT analysis. Pixels with $R^2 < 0.9$ have been discarded from further analysis. C, Angle f_c computed values. D, Anisotropy parameter B computed values. F, Angle f_2 values. G, Angle f_4 values

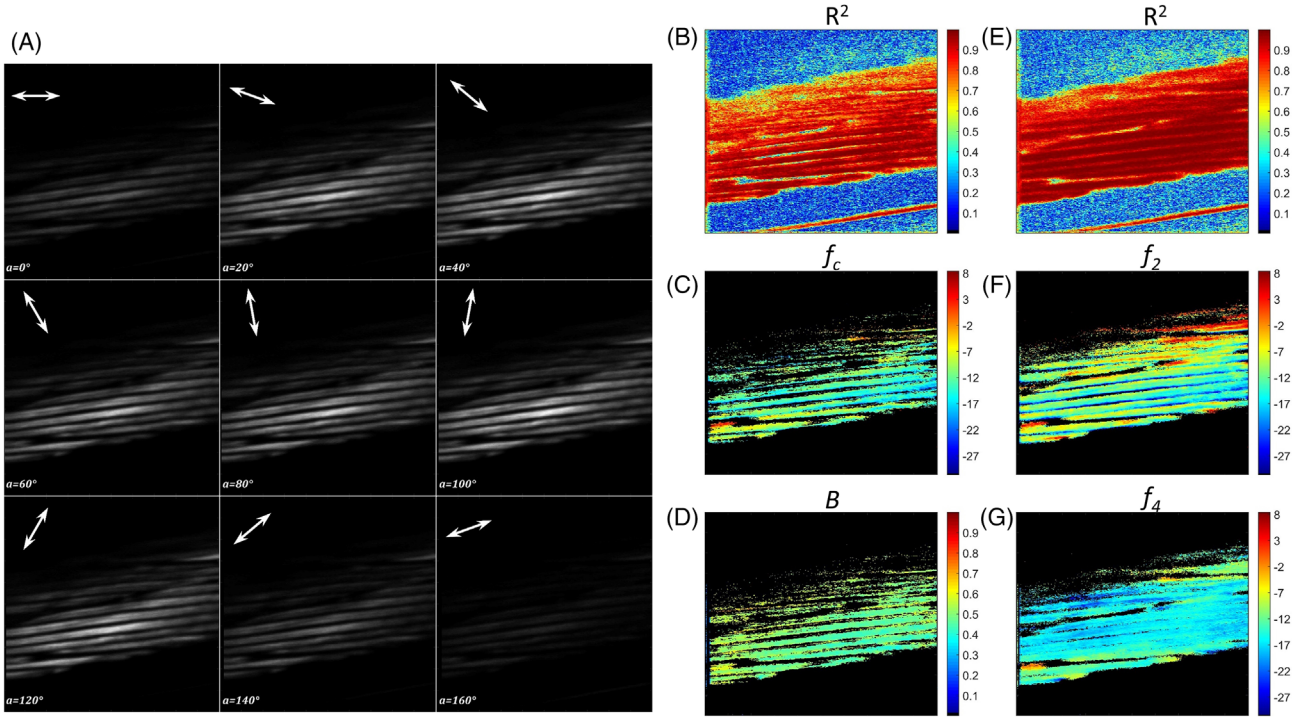

FIGURE 4 Results similar to those depicted in Figures 2 and 3 for a 9-day-old sample. The isolated red line at the bottom of B,E corresponds to SHG signal arising from collagen from the animal epidermis. These pixels are manually excluded from the other sub-images and from further processing

4 | DISCUSSION

The results of this study show that the anisotropy parameter B extracted by DFT analysis from the widely used cylindrical symmetry PSHG model does not present any changes across the *C. elegans* lifespan. So, it was not feasible by using this model for data analysis to detect myosin structural alterations during the aging of the worms. In addition, as Figure 7 presents the results from this model cannot adequately describe the PSHG data since the mean percentage of the pixels exhibit R^2 values higher than 0.9 is lower than 50%. The fitting procedure with the trigonal symmetry model appears improved mean ratio results and an increase of the mean DIF values during *C. elegans* lifespan. By using the most general form of I_{SHG} dependence with respect to the angle a (Equation (8)), the optimum score is obtained (up to 80%). The general model not only represents the PSHG data better but also the results of the DFT analysis based on this model that includes all possible structures provide an indication that the *C. elegans'* body striated muscles are undergoing structural modifications during aging. This indication is quantitatively expressed through the statistically significant increase of the mean DIF of the old (9d) compared with the young group of the worms (1d) (Figure 6). The DIF parameter for one sample defined as the average absolute difference of the angles f_2 and f_4, and this difference generally depends on the second-order tensor elements and thus to the sample's structure. For example, in the case of a cylindrical symmetric sample, the expected DIF value is zero, whereas in the case of a trigonal symmetry, the DIF value is estimated by Equations (17) and (18). Moreover, we showed that the observed raise of the DIF can be interpreted as an enhancement of the trigonal symmetry dominance to the cylindrical during aging. However, this does not imply that the younger samples should be exclusively described via a cylindrical symmetry model since they also present noticeable non-zero values of S (Figure 6B) and lower values of the ratio parameter compared to the other models (Figure 7).

The above indications about changes in *C. elegans* striated muscles structure can be correlated with the already known effects of sarcopenia on this organism. Sarcomeres of *C. elegans* exhibit progressive

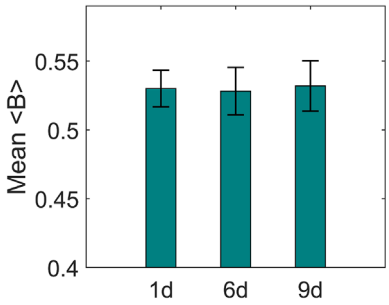

FIGURE 5 Mean <*B*> for 1-day, 6-days, and 9-days adult worms. The error bars are the SEM of each age group. $n = 12$ samples were irradiated in each case. The calculated B values are similar, and no significant difference is detected

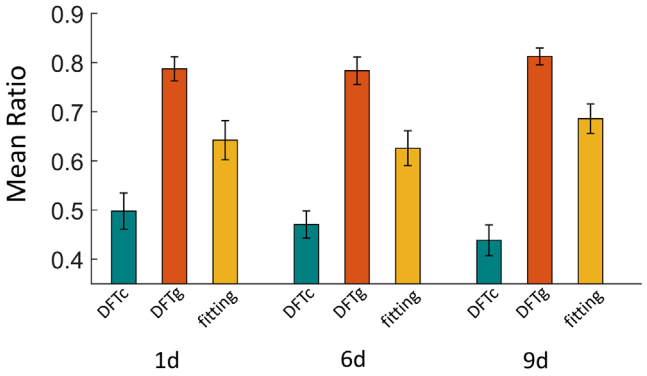

FIGURE 7 Mean ratio values for 1-day, 6-days, and 9-days adult samples obtained by: DFT analysis based on Equation (5) of cylindrical symmetry model (DFTc), DFT analysis based on Equation (8) of the general model (DFTg) and with the fitting procedure based on Equation (9) of the trigonal symmetry model. The error bars correspond to the SEM for each case. $n = 12$ specimens for each age group

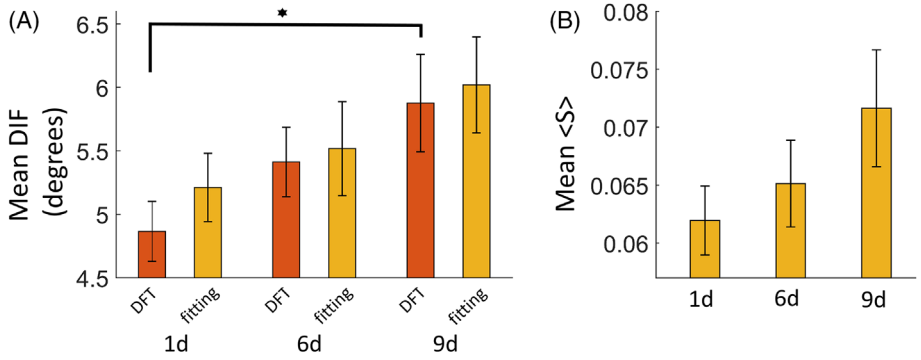

FIGURE 6 A, Mean DIF computed with DFT based on Equation (8) and estimated with a fitting procedure based on trigonal symmetry's Equations (9), (17) and (18) for the same samples as Figure 5. B, Mean <*S*> (symmetry parameter) resulting from fitting procedure of A. The error bars correspond to the SEM for each case. *Statistically significant (<.05)

disorganization, with less tight packing and some disorientation of myosin molecules with aging [3, 4]. In addition, a very recent study [17] has observed that there is a transition of SHG modulation with respect to the laser polarization in rat ventricles myosin filaments from a cylindrical to trigonal symmetry line profile during aging. The obtained results are in accordance with our study. They suggested that this transition may be due to changes in the ratio of α/β myosin isoforms ratio, which differ mainly in their head region. Nevertheless, as and in our case, it cannot be claimed that the detected changes in SHG modulation are exclusively arising from the enhancement of the presence of trigonal symmetry. Figure 7 demonstrates that for all the age groups the results of the DFT analysis based on the general model describe better the PSHG data. The following factors can interpret this behaviour: possible failure in the accurate determination of the total minimum during fitting procedure and/or the need for using an even more complicated model that takes into account more symmetries than the trigonal one.

5 | CONCLUSIONS

The development of label free, non-destructive techniques for the in-vivo monitoring and quantification of muscular changes at the sub-cellular level due to aging is a research field with high significance in biology. The findings presented herein suggest that the very promising modality of PSHG can be used as diagnostic tool for detecting myosin structural changes in the striated muscles of wild type *C. elegans* during their lifespan. It is not feasible to detect alterations and discriminate age groups via the implementation of the widely used, classical, cylindrical symmetry model and the calculation of the anisotropy parameter values. Nevertheless, the application of a trigonal symmetry or a general model for the analysis of the extracted PSHG data allows age classification of the nematodes based on the calculation of the difference between the angles f_2 and f_4 (DIF). Moreover, the obtained results suggest the enhancement of trigonal symmetry dominance over cylindrical symmetry in the striated muscles during the aging of the worms.

Further studies on mutants, such as animals with increased longevity or striated muscle defects, are expected to attribute additional insights for the thorough clarification of the morphological changes that the structure of the myosin molecules undergoes during aging. Beyond this, several muscle diseases are associated with sub-cellular changes in myosin molecules. Thus, in the near future, it would be very interesting and potentially useful to employ PSHG in studying the progression of these disorders, via the implementation of models that take into account more symmetries for the data processing and by employing state of the art, compact, user friendly setups.

ACKNOWLEDGMENTS

This work was supported by 'LASERLAB EUROPE V' (871124). Meropi Mari acknowledges the Hellenic Foundation for Research and Innovation (HFRI) and the General Secretariat for Research and Technology (GSRT), for the financial support under grant agreement No 1357. Vassilis Tsafas also acknowledges GSRT and HFRI for the financial support.

CONFLICT OF INTEREST

The authors declare no financial or commercial conflict of interest.

AUTHOR CONTRIBUTIONS

In the present study, Vassilis Tsafas performed the experiments and was assisted by Konstantina Giouroukou and Meropi Mari. All biological samples were prepared by Konstantinos Kounakis. Vassilis Tsafas was responsible for the data analysis. Costas Fotakis was involved in the conception of the work. Nektarios Tavernarakis and George Filippidis conceived and supervised the project. Vassilis Tsafas, Konstantinos Kounakis, Nektarios Tavernarakis and George Filippidis wrote this manuscript.

DATA AVAILABILITY STATEMENT

The data that support the findings of this study are available from the corresponding author upon reasonable request.

ORCID

George Filippidis https://orcid.org/0000-0003-4748-5968

REFERENCES

[1] V. Santilli, A. Bernetti, M. Mangone, M. Paoloni, *Clin. Cases Miner. Bone Metab.* **2014**, *11*, 177.
[2] L. V. Thompson, *Exp. Gerontol.* **2009**, *44*, 106.
[3] L. A. Herndon, P. J. Schmeissner, J. M. Dudaronek, P. A. Brown, K. M. Listner, Y. Sakano, M. C. Paupard, D. H. Hall, M. Driscoll, *Nature* **2002**, *419*, 808.
[4] C. F. Glenn, D. K. Chow, L. David, C. A. Cooke, M. S. Gami, W. B. Iser, K. B. Hanselman, I. G. Goldberg, C. A. Wolkow, *J. Gerontol. A Biol. Sci. Med. Sci.* **2004**, *59*, 1251.
[5] H. Kagawa, T. Takaya, R. Ruksana, F. Anokye-Danso, M. Z. Amin, H. Terami, *Advances in Experimental Medicine and Biology*. **2007**, *592*, 153.
[6] H. N. Aguilar, B. F. Mitchell, *Hum. Reprod. Update* **2010**, *16*, 725.

[7] P. Bianchini, A. Diaspro, *J. Biophotonics* **2008**, *1*, 443.
[8] S. V. Plotnikov, A. C. Millard, P. J. Campagnola, W. A. Mohler, *Biophys. J.* **2006**, *90*, 693.
[9] M. Pinsard, S. Laverty, H. Richard, J. Dubuc, M. C. Schanne-Klein, F. Légaré, *Sci. Rep.* **2019**, *9*, 1.
[10] V. Tsafas, E. Gavgiotaki, M. Tzardi, E. Tsafa, C. Fotakis, I. Athanassakis, G. Filippidis, *J. Biophotonics*. **2020**, *13*, e202000180. https://doi.org/10.1002/jbio.202000180.
[11] Z. Y. Zhuo, C. S. Liao, C. H. Huang, J. Y. Yu, Y. Y. Tzeng, W. Lo, C. Y. Dong, H. C. Chui, Y. C. Huang, H. M. Lai, S. W. Chu, *J. Struct. Biol.* **2010**, *171*, 88.
[12] G. Ducourthial, J. S. Affagard, M. Schmeltz, X. Solinas, M. Lopez-Poncelas, C. Bonod-Bidaud, R. Rubio-Amador, F. Ruggiero, J. M. Allain, E. Beaurepaire, M. C. Schanne-Klein, *J. Biophotonics* **2019**, *12*, e201800336.
[13] K. R. Campbell, R. Chaudhary, J. M. Handel, M. S. Patankar, P. J. Campagnola, *J. Biomed. Opt.* **2018**, *23*, 1.
[14] F. Tiaho, G. Recher, D. Rouède, *Opt. Express* **2007**, *15*, 12286.
[15] V. Nucciotti, C. Stringari, L. Sacconi, F. Vanzi, L. Fusi, M. Linari, G. Piazzesi, V. Lombardi, F. S. Pavone, *Proc. Natl. Acad. Sci.* **2010**, *107*, 7763.
[16] I. Amat-Roldan, S. Psilodimitrakopoulos, P. Loza-Alvarez, D. Artigas, *Opt. Express* **2010**, *18*, 17209.
[17] C. Yuan, X. Zhao, Z. Wang, T. K. Borg, T. Ye, Z. I. Khalpey, R. B. Runyan, Y. Shao, B. Z. Gao, *Biophys. J.* **2020**, *118*, 1058.
[18] C. Yuan, Z. Wang, T. K. Borg, T. Ye, C. Baicu, A. Bradshaw, M. Zile, R. B. Runyan, Y. Shao, B. Z. Gao, *Biomed. Opt. Express* **2019**, *10*, 3183.
[19] S. Brenner, *Genetics* **1974**, *77*, 71.
[20] E. Gavgiotaki, G. Filippidis, V. Tsafas, S. Bovasianos, G. Kenanakis, V. Georgoulias, M. Tzardi, S. Agelaki, I. Athanassakis, *Sci. Rep.* **2020**, *10*, 11055.
[21] W. L. Chen, T. H. Li, P. J. Su, C. K. Chou, P. T. Fwu, S. J. Lin, D. Kim, P. T. C. So, C. Y. Dong, *Appl. Phys. Lett.* **2009**, *94*, 183902.
[22] S. W. Chu, S. Y. Chen, G. W. Chern, T. H. Tsai, Y. C. Chen, B. L. Lin, C. K. Sun, *Biophys. J.* **2004**, *86*, 3914.
[23] P. Matteini, F. Ratto, F. Rossi, R. Cicchi, C. Stringari, D. Kapsokalyvas, F. S. Pavone, R. Pini, *Opt. Express* **2009**, *17*, 4868.
[24] J. Duboisset, D. Aït-Belkacem, M. Roche, H. Rigneault, S. Brasselet, *Phys. Rev. A* **2012**, *85*, 043829.
[25] X. Y. Dow, E. L. DeWalt, J. A. Newman, C. M. Dettmar, G. J. Simpson, *Biophys. J.* **2016**, *111*, 1553.
[26] R. Ambekar, T.-Y. Lau, M. Walsh, R. Bhargava, K. C. Toussaint, *Biomed. Opt. Express* **2012**, *3*, 2021.
[27] R. Mercatelli, S. Mattana, L. Capozzoli, F. Ratto, F. Rossi, R. Pini, D. Fioretto, F. S. Pavone, S. Caponi, R. Cicchi, *Commun. Biol.* **2019**, *2*, 1.
[28] R. Mercatelli, T. Triulzi, F. S. Pavone, R. Orlandi, R. Cicchi, *J. Biophotonics* **2020**, *13*, e202000159.
[29] V. Wasik, F. Galland, S. Brasselet, H. Rigneault, P. Réfrégier, *JOSA A* **2016**, *33*, 1353.
[30] V. Wasik, P. Réfrégier, M. Roche, S. Brasselet, *JOSA A* **2015**, *32*, 1437.
[31] A. H. J. Burr, C. Gans, *Biol. Bull.* **1998**, *194*, 1.

How to cite this article: V. Tsafas, K. Giouroukou, K. Kounakis, M. Mari, C. Fotakis, N. Tavernarakis, G. Filippidis, *J. Biophotonics* **2021**, *14*(12), e202100173. https://doi.org/10.1002/jbio.202100173